Proceedings of 8th International Conference on Mechanical Engineering and Renewable Energy 2025
10-12 December, 2025, Chattogram, BANGLADESH

SciEn Conference Series: Engineering Vol. 4, 2026, pp 525-530 https://doi.org/10.38032/scse.2026.4.233

Investigation of Ionizing Radiation Shielding and Mechanical Properties of Tin-Based Metal Alloys

Abdullah-Al-Mamun and M S Rabbi*

Department of Mechanical Engineering, Chittagong University of Engineering & Technology, Chattogram-4349, Bangladesh

ABSTRACT

The growing use of ionizing radiation in industrial, medical and nuclear sectors demands effective and eco-friendly shielding materials. In this study, Sn-based alloys (Sn-Cu-Ni, Sn-Ni-Zn, and Sn-Cu-Zn) were synthesized by stir casting and evaluated for their gamma-ray shielding and mechanical properties. Shielding performance was assessed with the EpiXS program, which provided parameters such as the mass and linear attenuation coefficients, mean free path, half-value layer, effective atomic number, and electron density across photon energies from 59.5 to 1332 keV, covering common sources including Am-241, Co-57, Ba-133, Cs-137, and Co-60. The computational results closely matched NIST XCOM values, with deviations below 0.32%. Among the alloys Sn-Cu-Zn performed best at low energies due to its higher atomic number, while Sn-Ni-Zn maintained balanced attenuation over the entire range. Mechanical testing indicated that Sn-Cu-Zn had the highest strength and hardness but limited toughness, whereas Sn-Cu-Ni showed superior impact resistance. Sn-Ni-Zn, though mechanically weaker, proved effective against high-energy photons. These results suggest that alloy composition can be tailored to meet specific shielding needs in diagnostic, therapeutic, or structural applications.

Keywords: Gamma shielding, EpiXS, Mechanical strength, Stir casting, Lead-free.

1. Introduction

Ionizing radiation (X-rays and gamma rays) plays a critical role in medical imaging, radiotherapy, nuclear engineering and industrial inspection. Yet exposure to such radiation poses health risks including cellular DNA damage and long-term carcinogenic effects, making radiation shielding a vital component of safety strategies [1-3]. Nuclear radiation safety follows the ALARA principle-minimizing exposure through time, distance, and shielding [4]. Traditional shielding materials like concrete, lead, Al, Fe, Cu and Pb slabs were widely used for their low cost and versatility with lead being highly effective against X- and γ-rays but limited by toxicity, hardness and secondary radiation [5]. Over the past decades, concrete, alloys, and glass have remained common in shielding equipment [6]. Protection strategies are either multi-layered or composite, where additives enhance density and performance as in modified concrete though achieving homogeneous mixtures can be challenging [7, 8]. Sometimes the uneven mixing of the compound also results in the production of tiny holes, through which radiation can pass [9]. Metallic coating technology uses multi-layer shielding to address this issue because it is an inexpensive technique to modify or control the base material's properties. The foundation material may be metallic, inorganic or organic such as paper, plastic or fiber 10].

Conventional shielding materials such as lead, concrete, and boron compounds are effective but limited by toxicity, weight and brittleness. Therefore, research is focusing on alternative materials that are mechanically robust, easy to fabricate and non-toxic [11][12].

Tin (Sn)-based alloys have emerged as promising shielding materials, with Cu, Ni, and Zn additions providing a balance of density for radiation attenuation and mechanical properties such as wear resistance and ductility [13] [14]. For example, Sn-Cu-Zn alloys show enhanced tensile strength and hardness compared to traditional bronzes [15], while Ni additions effectively strengthen Sn matrices through solid-solution hardening [16]. Microhardness and tensile properties improve with Zn and Cu content as shown in Sn-9 wt% Zn-2 wt% Cu solder alloys [13]. Mechanical efficacy of Sn-Cu-Zn alloys has been demonstrated in powder metallurgy bearing materials, with hardness ~55 BHN and compressive strength ~538 MPa [17]. Other studies, including molecular dynamics for Cu-Sn-Ni systems, show that Ni boosts tensile strength above 180 MPa with modest elongation [18]. Furthermore, Mg additions in Cu-Sn alloys significantly enhance hardness and strength [19]. Research on theoretical radiation shielding that employs resources like Phy-X/PSD, XCOM (NIST) and EpiXS has been crucial for forecasting essential factors such as the mass attenuation coefficient (MAC), linear attenuation coefficient (LAC), and half-value layer (HVL) across different energy spectra. These parameters are crucial for assessing how well materials protect against ionizing radiation [20]. Since Sn and Cu also contribute to effective atomic number, Sn-Cu-Zn and Sn-Cu-Ni materials are expected to perform well in shielding applications [21].

2. Materials and Method

2.1 Computational work

The mass attenuation coefficient (MAC) represents the probability of interaction between the material's mass per unit area and incident photons and it can be determined using

*Corresponding Author Email Address: amamun@cuet.ac.bd Published By: SciEn Publishing Group

the Ber–Lambert law as follows [22].

$$I = I_0 e^{-ut} \quad (1)$$

$$\mu_m = \frac{\mu}{\rho} = \frac{ln(I_0/I)}{\rho t} = \frac{ln(I_0/I)}{t_m} \quad (2)$$

where μ_m $[cm^2/g]$ and μ $[cm^{-1}]$ are mass and linear attenuation coefficients, respectively. The mass attenuation coefficient (MAC) for any compound can be obtained as follows.

$$\mu/\rho = \sum_i \omega_i (\mu/\rho)_i \quad (3)$$

Here, $(\mu/\rho)_i$ and ω_i denote the mass attenuation and the weight fraction coefficient of the *i-th* constituent element, respectively. The effective atomic number (Z_{eff}) is calculable as

$$Z_{eff} = \frac{\sigma_T}{\sigma_e} \quad (4)$$

Here, σ_e represents the electronic cross-section and σ_T denotes the total atomic cross-section of the sample, which can be expressed as

$$\sigma_e = \sum \frac{1}{Z_i} f_i (\sigma_T)_i \quad (5)$$

Here, f_i is the mole fraction of the *i-th* constituent element. An interpolation is then given by:

$$Z_{eff} = \frac{Z_1[\log(\sigma_2) - \log(\sigma_T)] + Z_2[\log(\sigma_T) - \log(\sigma_1)]}{\log(\sigma_2) - \log(\sigma_1)]} \quad (6)$$

This method can also serve for the explicit determination of Z_{eff}. In Eq. (6), σ_1 and $\sigma_2$represent the elemental cross-sections of two elements with atomic numbers Z_1 and Z_2, respectively. Other important parameters for analyzing the shielding features, such as the half-value layer (HVL), the tenth value layer (TVL) and the mean free path (MFP), are determined using the following relations.

$$HVL = \frac{\ln(2)}{\mu} \quad (7)$$

$$TVL = \frac{\ln(10)}{\mu} \quad (8)$$

$$MFP = \frac{1}{\mu} \quad (9)$$

LAC serves as one of the criteria for characterizing the interaction between photons and matter, and it is utilized to derive shielding parameters such as MAC, HVL, and MFP. The value of LAC depends on both MAC and the density of the compound. The density effect causes greater differences for LAC values compared with MAC values. Although this study employed XCOM and EpiXS software to determine these values, presenting the fundamental equations remains essential, as they form the theoretical basis of the computational tools and allow for validation and practical interpretation of the results. In this way, the connection between computational predictions and real-world shielding applications is maintained.

2.2 Stir Casting Method

The primary metal (Sn) is loaded into a crucible and heated in a resistance or induction furnace above its melting point (~232°C for Sn). Secondary metals (Ni, Cu, Zn) are added gradually. For metals with higher melting points (Ni, Cu), pre-melting separately or adding in small pieces helps avoid incomplete mixing. Once all metals are in molten form, a mechanical stirrer is used to create turbulent flow in the melt. Stirring ensures homogeneous distribution of all alloying elements. Stirring speed and duration depend on the melt viscosity and alloy composition (typically 300–600 rpm for 5–10 minutes. After the metal has melted, it is poured into molds to achieve the desired shape of the specimen. Once the molds solidified, the final samples were produced. After the composites are completely hardened, additional techniques like thread cutting, taper turning, grinding, and slot cutting need to be carried out. Thread-cutting and taper turning techniques were used to fabricate the tensile specimens. Slots were incorporated into the impact specimens. After all specified tasks were completed, final specimens were produced. The materials variation in the samples is shown in Table 1.

Table 1: Percentage composition of materials in the prepared samples.

Sample	Sn (wt.%)	Ni (wt%)	Zn (wt%)	Cu (wt%)
Sample 01 (S1)	50	25	-	25
Sample 02 (S2)	50	25	25	-
Sample 03 (S3)	50	-	25	25

Fig. 1 shows the dimensions of the tensile test specimen as specified by ASTM E8(American Society for Testing and Materials)

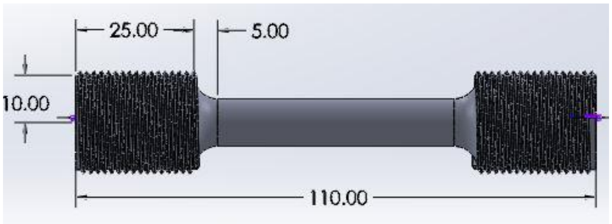

Fig. 1: Tensile test specimen.

The dimensions for the charpy V-notch impact test have been hown in Fig. 2 according to ASTM E23. The final appearance of the prepared samples is shown in Fig. 3.

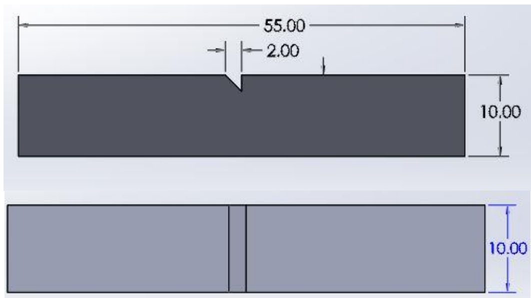

Fig. 2 Impact test Specimen

(a) (b) (c)

Fig. 3: Final specimens for a) Tensile test, b) Impact test, and c). Hardness test.

2.3 Density Measurement:

We determined the density of the alloy samples using Archimedes' principle and the formula.

$$\rho_{alloy} = \frac{m_a}{m_a - m_b} \times \rho_t \quad (10)$$

where m_a is the mass in air and m_b is the mass in fluid (toluene with density ρ_t = 0.867 $g\,cm^{-3}$). The mass of the samples immersed in toluene was measured using the setup shown in Fig. 4. The calculated density values have been presented in Table 2.

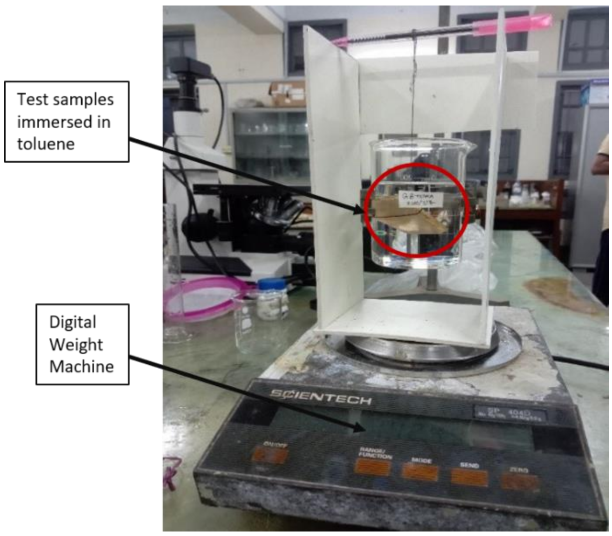

Fig. 4: Set-up for density measurement of samples immersed in toluene.

Table 2: Measured density of the alloys

Sample	Mass in air, m_a (gm)	Mass in Toluene m_b (gm)	ρ_{alloy}(g cm^{-3})
S1	62.86	56.461	8.517
S2	54.84	48.241	7.205
S3	61.57	55.071	8.214

2.4 Mechanical Properties evaluation

The experimental data was collected to generate a stress-strain curve, which was used to analyze the tensile behavior of the specimens in order to evaluate the mechanical properties of the alloys. A universal testing machine (UTM) was employed to measure the tensile strength. For the tensile testing, three samples were prepared and tested one after another under the same conditions. The following formulas were used to calculate tensile stress and cross-sectional area.

$$\sigma = \frac{F}{A} \quad (11)$$

$$A = \frac{\pi}{4} D^2 \quad (12)$$

A Brinell hardness tester was used to determine the hardness. In the Brinell hardness test, a tungsten carbide ball measuring 10 mm in diameter is placed on a flat surface of a workpiece and a constant force of 10 kN was applied for 10 seconds.

3. Results and Discussion

Standard gamma-ray sources including Am-241 (59.5 keV), Co-57 (122 keV), Ba-133 (356 keV), Cs-137 (662 keV) and Co-60 (1173 and 1332 keV) were employed for theradiation shielding analysis. All shielding parameters (Presented in Tables 3-4) and corresponding graphs (Figs. 5-7) were obtained using EpiXS based on EPICS2017 data and compared with reference data retrieved from NIST XCOM. Figs. 5-7 show the change of MAC values for S1, S2, and S3 along with photon energy. At low photon energies (59.5-122 keV), Sample S3 exhibited the highest MAC and LAC values, along with the lowest MFP and HVL showed in Table 3 and Table 4. This performance is attributed to its relatively higher Zeff and electron density which enhance photoelectric absorption. Conversely, S1 showed comparatively lower attenuation performance at these energies. In the intermediate-to-high photon energy range (356-1332 keV), Sample S2 demonstrated consistently higher attenuation coefficients and favorable shielding parameters compared to S1 and S3. The addition of Ni contributes to improved photon interaction probability through Compton scattering, making S2 the most effective for broad-spectrum gamma shielding. If we go beyond 1.3 MeV the MAC graphs of all three samples are almost identical.

Overall, S2 provides the most balanced performance, exhibiting slightly higher MAC values at intermediate to high photon energies (up to 1332 keV), whereas S3 demonstrates superior attenuation at very low energies (59.5–122 keV).

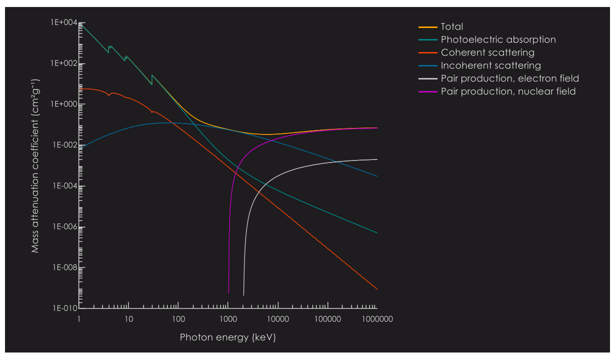

Fig. 5: MAC of S1 as a function of photon energy.

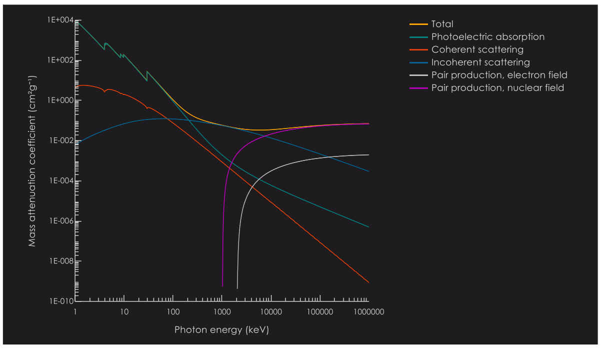

Fig. 6: MAC of S2 as a function of photon energy.

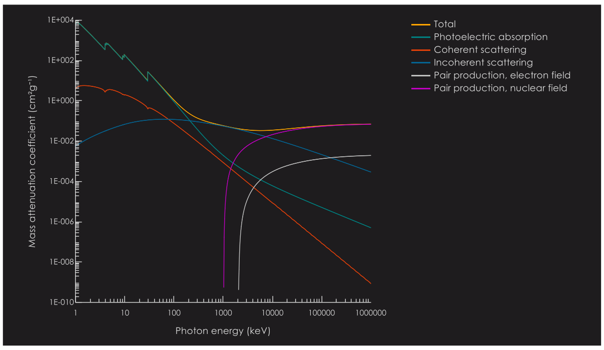

Fig. 7: MAC of S3 as a function of photon energy.

Table 3: MAC, LAC and MFP of the three samples at selected photon energies.

Samples	**Energy (keV)**	**MAC (cm^2g^{-1})**	**LAC (cm^{-1})**	**MFP (cm)**
S1	59.5	4.1618	35.446	0.02821
	122	0.6587	5.610	0.17824
	356	0.1168	0.995	1.00501
	662	0.0747	0.637	1.57091
	1173	0.0541	0.460	2.17190
	1332	0.0505	0.430	2.32300
S2	59.5	4.2049	30.296	0.03301
	122	0.6643	4.786	0.20893
	356	0.1172	0.845	1.18402
	662	0.0749	0.540	1.85331
	1173	0.0541	0.390	2.56328
	1332	0.0506	0.365	2.74166
S3	59.5	4.2256	34.709	0.02881
	122	0.6657	5.469	0.18286
	356	0.1163	0.956	1.04648
	662	0.0741	0.6089	1.64244
	1173	0.0535	0.4399	2.27342
	1332	0.0501	0.4112	2.43173

Table 4: HVL, Zeff and Neff of the three samples at selected photon energies.

Samples	Energy (keV)	Half value layer (cm)	Zeff	Neff ($\times 10^{23}$ electrons g^{-1})
S1	59.5	0.019555	39.53237	2.953376
	122	0.123548	39.67072	2.963712
	356	0.696623	38.06869	2.844028
	662	1.088870	36.78684	2.748264
	1173	1.505450	36.24146	2.70752
	1332	1.610180	36.19404	2.703978
S2	59.5	0.022879	39.73504	2.942141
	122	0.144816	39.87267	2.952333
	356	0.820699	38.36018	2.840341
	662	1.284610	37.12805	2.749109
	1173	1.776730	36.60013	2.710021
	1332	1.900370	36.55406	2.706609
S3	59.5	0.019970	40.07102	2.888526
	122	0.126747	40.21419	2.898847
	356	0.725365	38.81582	2.798045
	662	1.138450	37.65137	2.714106
	1173	1.575820	37.14017	2.677255
	1332	1.685550	37.09447	2.673961

The relative differences between the EpiXS and XCOM mass attenuation coefficients (MACs) for the three samples were evaluated across representative photon energies (59.5–1332 keV). At lower energies (59.5–122 keV), EpiXS values were slightly higher than XCOM, with positive deviations of approximately 0.25–0.3%. In the intermediate range (356–662 keV), EpiXS MACs were marginally lower, with differences between –0.06% and –0.16%. At higher energies (1173–1332 keV), the negative deviation increased slightly, reaching –0.17% to –0.23%. Overall, the maximum relative difference did not exceed 0.32%, indicating good agreement between the two datasets across the full energy range.

Table 5: Relative differences (%) between EpiXS and NIST XCOM MAC values for the alloys at selected photon energies.

Sources	**Energy (keV)**	**S1 (%)**	**S2 (%)**	**S3 (%)**
Am-241	59.5	0.260901	0.259895	0.251483
Co-57	122	0.307751	0.319843	0.313545
Ba-133	356	-0.0633	-0.0665	-0.14077
Cs-137	662	-0.14482	-0.16118	-0.15679
Co-60	1173	-0.16694	-0.17257	-0.16648
Co-60	1332	-0.23016	-0.2294	-0.23037

The mechanical properties of the three selected alloys are summarized in Table 5. Fig. 8 shows the stress-strain curves of the alloys, Fig. 9 illustrates the hardness measurements and Fig. 10 presents their impact strength. Among all the samples, S3 exhibited the highest tensile strength (185.79 MPa) and hardness (96.7 HB) but a relatively low impact strength (24.1 J/cm²). This indicates a microstructure optimized for rigidity and resistance to deformation, likely due to higher Cu content, which is well-documented to enhance strength and hardness through solid solution and precipitation strengthening [23]. However, this comes at the expense of ductility and toughness, as reflected in the low impact strength- a typical outcome when maximizing strength in metallic alloys. S1 showed moderate tensile strength (162.97 MPa) and hardness (90.3 HB) while maintaining the highest impact strength (67.3 J/cm²), reflecting a balanced combination of strength and toughness. S2 displayed the lowest tensile strength (150.24 MPa), hardness (45.1 HB) and impact strength (18.4 J/cm²). Researchers found, while Ni can improve ductility and toughness at moderate levels, its strengthening effect is less pronounced when the Sn matrix dominates. Ni's ability to form hard intermetallics is less effective in a high-Sn environment, leading to lower overall strength[24]. Zn can refine microstructure and enhance strength and hardness, but its optimal effect is seen at lower additions (typically <0.5–2% in Sn-based alloys). At higher concentrations, Zn may not further improve, and can even disrupt, the microstructural balance, leading to coarser phases and reduced mechanical properties [25].

Table 5: Mechanical properties (tensile strength, hardness, and impact toughness) of the selected alloys.

Sample	Tensile strength (MPa)	BHN (HB)	Impact strength (J/cm^2)
S1	162.97	90.3	67.3
S2	150.24	45.1	18.4
S3	185.79	96.7	24.1

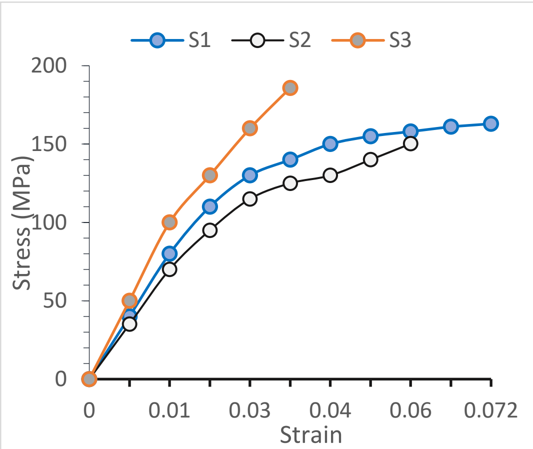

Fig. 8: Stress-Strain Curves of the selected alloys.

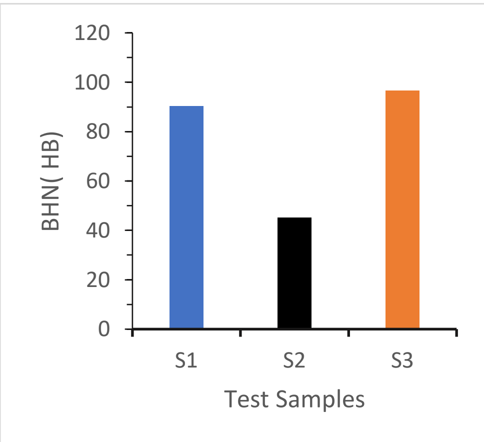

Fig. 9: Brinell Hardness Number of the alloy samples.

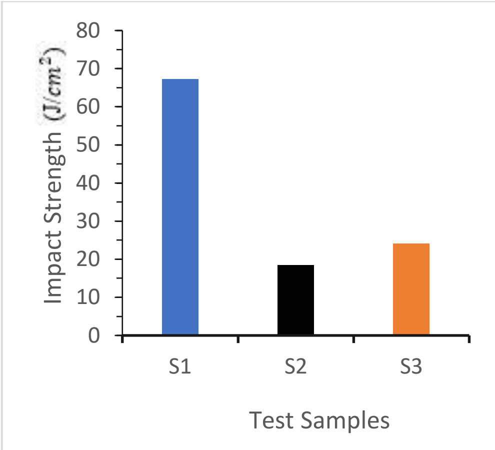

Fig. 10: Impact Strength of the alloy samples.

4. Conclusions

This study demonstrates that Sn-based alloys can be used for both radiation shielding and mechanical performance. S3 (Sn-Cu-Zn) showed superior low-energy gamma-ray attenuation and high strength and hardness, making it suitable for diagnostic shielding applications. S2 (Sn-Ni-Zn) offered balanced shielding across medium and high energies, ideal for radiotherapy and nuclear environments, though with lower mechanical strength. S1(Sn-Cu-Ni) provided moderate shielding but excellent impact toughness, suitable for portable or structural shielding components. Alloying with Cu, Ni and Zn significantly influences the balance between strength, hardness and ductility, highlighting the potential to optimize composition for specific applications. Future work should focus on experimental validation of shielding performance, microstructural studies, long-term irradiation stability and the development of eco-friendly or composite Sn-based shields as sustainable alternatives to lead-based materials.

5. References

[1] A. Samarin, "Use of concrete as a biological shield from ionising radiation," *Sustain. Constr. Mater. Technol.*, vol. 2013-Augus, no. 2, pp. 90–97, 2013

[2] L. Huang and Z. Fu, "Effect of Al Content on Microstructure and Mechanical Behavior of AsCastNi35(CoCr)62-xAlxTi3High-Entropy Alloys,"

75th World Foundry Congr. WFC 2024, pp. 154–155, 2024

[3] Z. X. Zhao *et al.*, "Effect of Sn content on the microstructure, mechanical properties and corrosion behavior of biodegradable Mg-x (1, 3 and 5 wt.%) Sn-1Zn-0.5Ca alloys," *Materials (Basel).*, vol. 11, no. 12, pp. 1–14, 2018

[4] I. Akkurt, H. Akyildirim, B. Mavi, S. Kilincarslan, and C. Basyigit, "Gamma-ray shielding properties of concrete including barite at different energies," *Prog. Nucl. Energy*, vol. 52, no. 7, pp. 620–623, 2010

[5] A. M. Reda and A. A. El-Daly, "Gamma ray shielding characteristics of Sn-20Bi and Sn-20Bi-0.4Cu lead-free alloys," *Prog. Nucl. Energy*, vol. 123, p. 103304, 2020

[6] U. Perişanoğlu, E. Kavaz, H. O. Tekin, S. R. Armoosh, N. Ekinci, and M. Oltulu, "Comparison of gamma and neutron shielding competences of Fe–Cu- and brass-added Portland cement pastes: an experimental and Monte Carlo study," *Appl. Phys. A*, vol. 126, no. 6, p. 470, 2020

[7] E.-S. A. Waly, M. A. Fusco, and M. A. Bourham, "Gamma-ray mass attenuation coefficient and half value layer factor of some oxide glass shielding materials," *Ann. Nucl. Energy*, vol. 96, pp. 26–30, 2016, doi: https://doi.org/10.1016/j.anucene.2016.05.028.

[8] M. Arif Sazali, N. K. Alang Md Rashid, and K. Hamzah, "A review on multilayer radiation shielding," *IOP Conf. Ser. Mater. Sci. Eng.*, vol. 555, no. 1, 2019

[9] Y. Kim, S. Park, and Y. Seo, "Enhanced X-ray Shielding Ability of Polymer–Nonleaded Metal Composites by Multilayer Structuring," *Ind. Eng. Chem. Res.*, vol. 54, no. 22, pp. 5968–5973, Jun. 2015

[10] S. Park, H. Kim, Y. Kim, E. Kim, and Y. Seo, "Multilayer-Structured Non-leaded Metal/Polymer Composites for Enhanced X-ray Shielding," *MRS Adv.*, vol. 3, no. 31, pp. 1789–1797, 2018

[11] S. K. Das and S. H. Dhobi, "Radiation Shielding Properties of Nickel, Copper and Iron Based Alloys," *Patan Prospect. J.*, vol. 4, no. 01, pp. 118–134, 2024

[12] T. Wu *et al.*, "Enhanced mechanical strength of Cu-Sn alloy by Mg addition," *Mater. Res. Express*, vol. 8, no. 1, 2021

[13] B. L. Silva and J. E. Spinelli, "Correlations of microstructure and mechanical properties of the ternary Sn-9wt%Zn2wt%Cu solder alloy," *Mater. Res.*, vol. 21, no. 2, pp. 1–9, 2018

[14] C. V. More, Z. Alsayed, M. S. Badawi, A. A. Thabet, and P. P. Pawar, *Polymeric composite materials for radiation shielding: a review*, vol. 19, no. 3. Springer International Publishing, 2021

[15] S. E. Susilowati, A. Fudholi, and D. Sumardiyanto, "Mechanical and microstructural characteristics of Cu–Sn–Zn/ Gr metal matrix composites processed by powder metallurgy for bearing materials," *Results Eng.*, vol. 14, no. February, p. 100377, 2022

[16] W. Gao, D. Cao, Y. Jin, X. Zhou, G. Cheng, and Y. Wang, "Composite Coatings on Mild Steel," pp. 1–21.

[17] C. Hou *et al.*, "Microstructure and Mechanical Properties of As-Aged Mg-Zn-Sn-Mn-Al Alloys," *Materials (Basel).*, vol. 16, no. 1, pp. 1–16, 2023

[18] S. U. Ayuba, O. S. I. Fayomi, and O. A. Omotosho, "Experimental investigation of nanomechanical response from synergistic metal alloy fusion of Cu-Al-Zn-Sn for anti-corrosion and structural application," *Int. J. Adv. Manuf. Technol.*, vol. 132, no. 11–12, pp. 5621–5632, 2024

[19] K. Maki, Y. Ito, H. Matsunaga, and H. Mori, "Solid-solution copper alloys with high strength and high electrical conductivity," *Scr. Mater.*, vol. 68, no. 10, pp. 777–780, 2013

[20] E. Şakar, Ö. F. Özpolat, B. Alım, M. I. Sayyed, and M. Kurudirek, "Phy-X / PSD: Development of a user friendly online software for calculation of parameters relevant to radiation shielding and dosimetry," *Radiat. Phys. Chem.*, vol. 166, p. 108496, 2020

[21] K. M. Abdulazeez and W. A. Sheekhoo, "Synergistic radiation shielding performance of Cu-based ternary alloys for multifunctional gamma , beta , and neutron radiation protection," vol. 123, pp. 29–39, 2025.

[22] G. F. Knoll, *Radiation detection and measurement*. New York, NY: Wiley, 2010. [Online]. Available: https://cds.cern.ch/record/1300754

[23] M. Mikolajčík, L. Kuchariková, E. Tillová, J. M. Sanchez, Z. Šurdová, and M. Chalupová, "Influence of Copper Addition on the Mechanical Properties and Corrosion Resistance of Self-Hardening Secondary Aluminium Alloy AlZn10Si8Mg," *Metals (Basel).*, vol. 14, no. 7, 2024

[24] I. N. Qader, M. Kok, and Z. D. Cirak, "The effects of substituting Sn for Ni on the thermal and some other characteristics of NiTiSn shape memory alloys," *J. Therm. Anal. Calorim.*, vol. 145, no. 2, pp. 279–288, 2021

[25] B. Alloy, "Babbitt Alloy," 2024.